Journal of Materials Chemistry A

Thermal Deposition Method for p–n Patterning of Carbon Nanotube Sheets for Planar-type Thermoelectric Generator

Journal:	*Journal of Materials Chemistry A*
Manuscript ID	TA-ART-03-2021-002206.R1
Article Type:	Paper
Date Submitted by the Author:	04-May-2021
Complete List of Authors:	Fujigaya, Tsuyohiko; Kyushu Daigaku Kogakubu Daigakuin Kogakufu, Yamaguchi, Ryohei; Kyushu Daigaku Kogakubu Daigakuin Kogakufu, Ishii, Taiki; Kyushu University Matsumoto., Masamichi; Kyushu Daigaku Kogakubu Daigakuin Kogakufu Angana, Borah; Kyushu Daigaku Kogakubu Daigakuin Kogakufu Tanaka, Naoki; Kyushu University, Applied Chemistry Oda, Kaito; Waseda University Tomita, Motohiro; Waseda University, Research Institute for Ambientornic Watanabe, Takanobu; Waseda Univeristy

ARTICLE

Thermal Deposition Method for p–n Patterning of Carbon Nanotube Sheets for Planar-type Thermoelectric Generator

Received 00th January 20xx,
Accepted 00th January 20xx

DOI: 10.1039/x0xx00000x

Ryohei Yamaguchi,[a] Taiki Ishii,[a] Masamichi Matsumoto,[a] Angana Borah,[a] Naoki Tanaka,[ad] Kaito Oda,[b] Motohiro Tomita,[bc] Takanobu Watanabe,[bc] and Tsuyohiko Fujigaya,*[ade]

Thermoelectric generators (TEGs) using flexible single-walled carbon nanotube (SWCNT) sheets have a high Seebeck coefficient, remarkable electrical conductivity, and good flexibility, making them promising for the realization of wearable electronics. TEGs with a planar structure are preferable to those with π-shaped structures, as the planar surface enables the device to be attached flat to a surface such as skin. To realize a planar configuration, sequentially repeating p- and n-type areas must be fabricated with high precision. However, there is considerable molecular diffusion in the lateral directions when using solution doping methods, which decreases the patterning resolution. Therefore, in this study, a dry patterning process is developed based on thermal vapor deposition using patterned masks. For the patterning, p-type SWCNT sheets are doped using 2-(2-methoxyphenyl)-1,3-dimethyl-1*H*-benzoimidazol-3-ium iodide as the n-type dopant. The 50-μm-thick SWCNT sheets are doped from the top to the bottom of the sheet with a lateral diffusion of only ~100 μm. Planar SWCNT-based TEGs with four p–n units exhibit an efficient power generation of 60 nW cm^{-2} (at ΔT = 25 °C), with scope for further optimization via simulation-based design.

1. Introduction

Wearable flexible electronics with sensors and displays are key components for realizing the Internet of Things.[1-6] Thermoelectric generators (TEGs) are a promising technology for supplying power to these devices, as they produce electricity from a heat gradient, thereby limiting the need for recharging.[7-10] To obtain TEGs with a high conversion efficiency, a large power factor (PF; determined by PF = $S^2\sigma$, where S and σ are the Seebeck coefficient and electrical conductivity, respectively) is preferable. Various TEG materials, particularly inorganic semiconductors such as Bi_2Te_3, have been extensively studied[11-16] because of their high PF of over 1.0 mW m^{-1} K^{-2} near room temperature.[17-20] However, these inorganic materials often lack flexibility and processability. Thus, complex device configurations such as Origami structures have been developed.[21]

Recently, single-walled carbon nanotubes (SWCNTs) have emerged as a candidate material for TEGs owing to their excellent electrical conductivity, mechanical strength, good flexibility, and processability.[22, 23] However, their PF is limited to approximately 300 μW m^{-1} K^{-2} when unsorted (mixture of semiconducting and metallic) SWCNTs are used;[24-26] thus, the integration of multiple TEG units into a single device is required. Typically, integration is achieved with a π-type configuration (Fig. 1a), in which a number of p- and n-type SWCNT sheets or fibers are connected alternatively in a zigzag pattern.[27-29] However, because the hot side must be separated from the cool side to create the temperature gradient, the π-type configuration must be attached vertically to the hot surface, which is undesirable for producing compact wearable devices. To overcome this issue, we developed a novel planar configuration for silicon-based TEG materials,[30] in which heat injection is spatially regulated by the placement of thermal conductors to generate a temperature gradient in the in-plane direction (Fig. 1b). In this configuration, the integration of multiple p–n sequences is possible in a single SWCNT sheet by alternate patterning of p- and n-type regions, with thermal conductors attached at alternate p–n junctions. This is expected to increase the power density while retaining a simple structure. In addition, in the planner-type structure, the TEG sheets can be attached on the surface of heat source without folding the sheets, while p-type structure needs to fold the sheets in zigzag shape and attach them on the heat source perpendicularly to make the other side of the sheet cooler. Therefore, planner-type TEG structure is much preferable for the wearable applications. Since SWCNT sheets generally have a p-type nature, the patterning of n-type regions on a p-type SWCNT sheet will enable the fabrication of such a structure.

[a] Department of Applied Chemistry, Graduate School of Engineering, Kyushu University, 744 Motooka, Nishi-ku, Fukuoka 819-0395, Japan.
[b] Faculty of Science and Engineering, Waseda University, 3-4-1 Ookubo, Shinjuku-ku, Tokyo 169-8555, Japan.
[c] Research Institute for Ambientornics, Waseda University, 3-4-1 Ookubo, Shinjuku-ku, Tokyo, 169-8555, Japan.
[d] International Institute for Carbon Neutral Energy Research (WPI-I2CNER), Kyushu University, Fukuoka 819-0395, Japan.
[e] Center for Molecular Systems (CMS), Kyushu University, 744 Motooka, Nishi-ku, Fukuoka 819-0395, Japan.

†Electronic Supplementary Information (ESI) available: [Additional schemes, XPS survey scans of the SWCNT sheets, Photograph of the mask, Thermal conductivity mapping of the patterned SWCNT sheet, Plot of OCV and circuit resistance for TEGs, and List of the performance for SWCNT-based TEGs]. See DOI: 10.1039/x0xx00000x

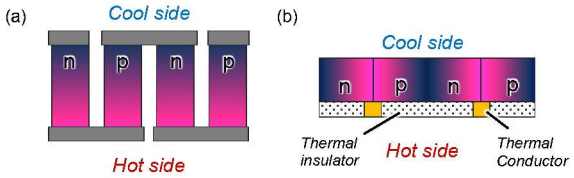

Fig. 1 Schematic of (a) π-type and (b) planar TEG structure.

To date, a wide range of organic n-dopant molecules have been developed,[31] including crown ether salts,[32, 33] benzimidazole derivatives,[34-38] polyethyleneimine,[39, 40] cobaltocene[41] and benzyl viologen.[42, 43] The doping of SWCNT sheets with these molecules has been carried out via solution-based wet processes, whereby the SWCNT sheet is dipped into the dopant solution, or the dopant solution is cast onto the SWCNT sheet. However, it is difficult to regulate the patterning area with wet processes as the solution tends to diffuse laterally into the SWCNT sheet.[44]

In this study, we demonstrate the precise p–n patterning of an SWCNT sheet through thermal vapor deposition. We chose 2-(2-methoxyphenyl)-1,3-dimethyl-1*H*-benzoimidazol-3-ium iodide (*o*-MeO-DMBI-I) as an n-dopant.[45, 46] Previously, Bao et al. reported the n-doping of a thin fullerene film (30 nm thick)[47] and a thin SWCNT sheet (1.5 nm thick)[45] by a similar thermal vapor deposition method using *o*-MeO-DMBI-I as a dopant. In these systems, *o*-MeO-DMBI-I generates *o*-MeO-DMBI radicals upon thermal deposition and forms *o*-MeO-DMBI cations after electron transfer to the substrate.[46] Thus, this dry process is expected to be suitable for the precise patterning of n-type regions on SWCNT sheets. In addition, the doping based on thermal deposition allows us to make p-n patterns at once when using slit mask, while the patterning based on solution casting or painting need multiple doping. However, the vertical (through-plane) and lateral (in-plane) diffusion of dopants in thicker films have not been studied. Here, we studied the patterning of *o*-MeO-DMBI-I on thick SWCNT sheets (~50 μm thick) to study the through-plane and in-plane diffusion. The p–n patterned SWCNT sheets were used to produce planar TEG cells and the power density of this device was measured.

2. Results and discussion

Dopant diffusion in through-plane direction

The thermal deposition of *o*-MeO-DMBI-I onto SWCNT sheets (50 μm thick) was carried out under vacuum (10^{-3} Pa) at a heating temperature of 180 °C (Fig. 2a) to induce n-doping. Fig. 2b shows the temperature dependence of the in-plane Seebeck coefficient of the SWCNT sheets without (black) and with (red) thermal deposition of *o*-MeO-DMBI-I. The Seebeck coefficient of the non-doped SWCNT sheet was roughly constant at approximately +54 μV K^{-1}. In contrast, the deposited SWCNT sheet had a Seebeck coefficient of +20 μV K^{-1} at 30 °C, indicating that slight n-doping of the SWCNT sheet was achieved by thermal deposition. Moreover, the Seebeck coefficient gradually reduced as the temperature increased, and it became negative after heating to above 60 °C. Therefore, heating above 60 °C might promote the doping reaction as further discussed later. Thus, the thermal deposition process was followed by a post heat-treatment at 80 °C for 90 min to achieve full n-doping. After post heating, the Seebeck coefficient became −54 μV K^{-1} (red plots in Fig. 2c, for their electrical conductivity and power factor, see Fig. S1). Interestingly, the Seebeck coefficient of the back side of the post-heated (denoted as 'doped') SWCNT

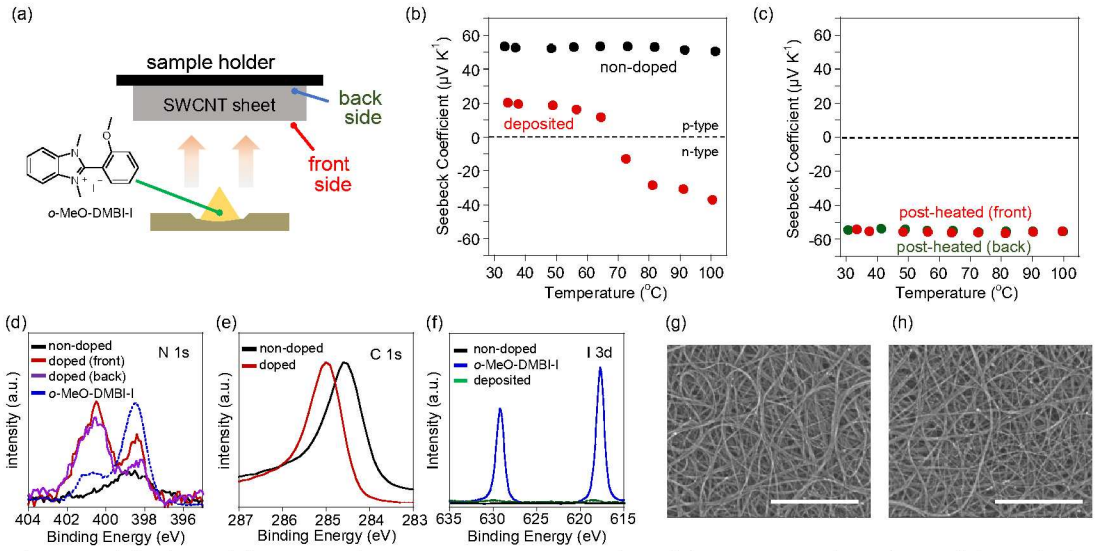

Fig. 2 (a) Schematic of the thermal deposition of *o*-MeO-DMBI-I on SWCNT sheet. (b) Temperature dependence of the Seebeck coefficient of the SWCNT sheets without (black) and with (red) the thermal deposition of *o*-MeO-DMBI-I. (c) Temperature dependence of the Seebeck coefficient for the front (red) and back (green) sides of the doped SWCNT sheet. XPS narrow scans of (d) N 1s, (e) C 1s, and (f) I 3d for *o*-MeO-DMBI-I (blue), the SWCNT sheets without (black) and with (green) the thermal deposition of *o*-MeO-DMBI-I, the front (red) and back (purple) sides of the post-heated (doped) SWCNT sheets.

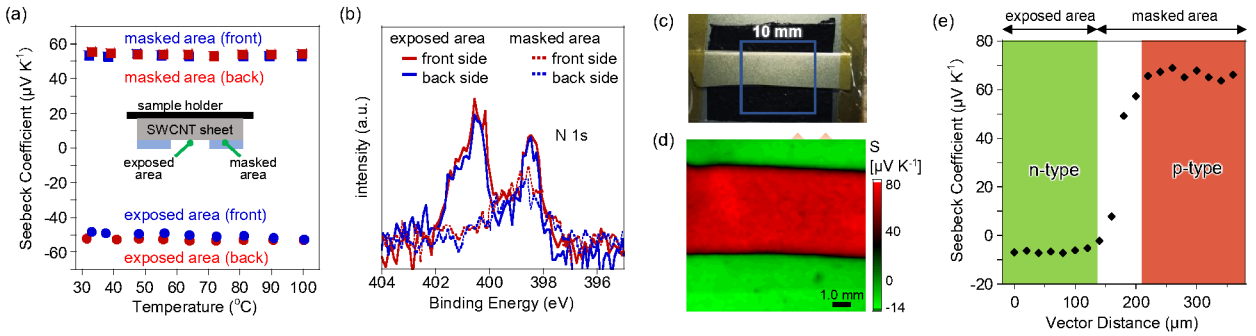

Fig. 3 (a) Temperature dependence of the Seebeck coefficient of exposed (filled circles) and masked (filled squares) areas for the front (red) and back (blue) sides of SWCNT sheets after thermal deposition of *o*-MeO-DMBI-I and post heating. Inset: Side view schematic of the masked SWCNT sheet. (b) N 1s XPS scans of the exposed (solid line) and masked (dotted line) areas on the front (red) and back (blue) sides of SWCNT sheets. (c) Top view photograph of the masked SWCNT sheet. (d) Seebeck coefficient mapping of the SWCNT sheet after thermal deposition of *o*-MeO-DMBI-I and post heating. (e) Plot of the Seebeck coefficient at the boundary between masked (p-type) and unmasked (n-type) areas.

sheets was also −55 μV K^{-1} (green plots in Fig. 2c). This result demonstrates that the dopant molecules diffused evenly through the sheets in the through-plane direction and confirms that n-doping can be successfully carried out in thick SWCNT sheets (50 μm thick).

N 1s, C 1s, and I 3d X-ray photoelectron spectroscopy (XPS) data of the doped and non-doped SWCNT sheets are presented in Fig. 2d–f. The N 1s and I 3d spectra of *o*-MeO-DMBI-I are also shown. (For survey scans, see Fig. S2†) In the N 1s spectra (Fig. 2d), characteristic peak for the n-doping of *o*-MeO-DMBI at 400.5 eV (cationic N=) [35] became intense compared to the peak at 398.5 eV (N–) for both the front and back sides of the doped SWCNT sheets (red and purple lines, respectively). This result clearly supports the through-plane diffusion of dopant molecules through the SWCNT sheet. In the C 1s spectra (Fig. 2e), the peak at 284.6 eV upshifted to 285.0 eV after doping, corresponding to an upshift of the Fermi level by electron doping.[48-50] The 0.4 eV shift is comparable to the band gap of semiconducting SWCNTs with a diameter of 1.5 nm (ca. 0.45 eV);[51] thus, the observed shift further verifies that n-type doping of the SWCNTs was achieved. In the I 3d spectra (Fig. 2f), the peaks at 618 and 629 eV (corresponding to I $3d_{5/2}$ and I $3d_{3/2}$, respectively) for *o*-MeO-DMBI-I (blue line) were dramatically decreased after the deposition (green line). This result supports the loss of iodide during thermal deposition, as reported previously.[52] Fig. 2g and 2h show scanning electron microscopy (SEM) images of non-doped and doped SWCNT sheets, respectively. The network structures formed by the SWCNT bundles showed no obvious changes after doping, and the thermal deposition of *o*-MeO-DMBI-I did not alter the SWCNT morphology.

Dopant diffusion in in-plane direction

The in-plane diffusion of the dopant molecules was studied by applying a slit-shaped mask (slit size: 2 mm × 18 mm, Fig. S3†) to the SWCNT sheet prior to the doping process (thermal deposition of *o*-MeO-DMBI-I and post heating), as illustrated in the inset of Fig. 3a. After doping, the sheets were sectioned to isolate the exposed area (2 mm × 18 mm) and masked area (2 mm × 18 mm) for further Seebeck coefficient analysis and XPS measurements. Fig. 3a shows the temperature dependence of the Seebeck coefficient of the masked and exposed SWCNT specimens. The exposed area had a Seebeck coefficient of −52 μV K^{-1} on the front side (red filled circles) and −48 μV K^{-1} on the back side (blue filled circles). In contrast, the masked area had Seebeck coefficients of 56 and 54 μV K^{-1} on the front and back sides, respectively (red and blue open circles, respectively). N 1s XPS scans of the two specimens (Fig. 3b) revealed that both the front and back sides of the unmasked area (red and blue solid lines, respectively) exhibited peaks at 398.5 and 400.5 eV, which correspond to the *o*-MeO-DMBI cation. On the other hand, these peaks were not detected for the masked area on either side (red and blue dotted lines). The above results suggest that lateral diffusion was not significant, and the diffusion was well regulated in the in-plane direction, which is preferable for achieving precise patterning of n-doped areas on the SWCNT sheet.

The spatial resolution of the patterning was further analyzed using scanning thermal probe imaging in the boundary region (Fig. 3c) to create mapping images of the Seebeck coefficient (Fig. 3d) and thermal conductivity (Fig. S4†). The masked and exposed areas were clearly differentiated, with Seebeck coefficients of approximately +70 and −10 μV K^{-1}, respectively (Fig. 3e). It is noted that these values are different from the values obtained in the bulk measurements as shown in Fig. 2b and 2c (approx. +50 and −50 μV K^{-1} for p- and n-type, respectively). These differences were likely due to the interfacial thermal resistances at probe/SWCNT sheet and substrate/SWCNT sheet, which were not considered in the calculation (Fig. S5†). Fig. 3e depicts a plot of the Seebeck coefficient near the boundary area. Notably, the boundary length of the Seebeck coefficient is approximately 100 μm, demonstrating the sharp contrast of this method to solution-based doping, which suffers from centimeter-scale diffusion.[44]

Doping mechanism

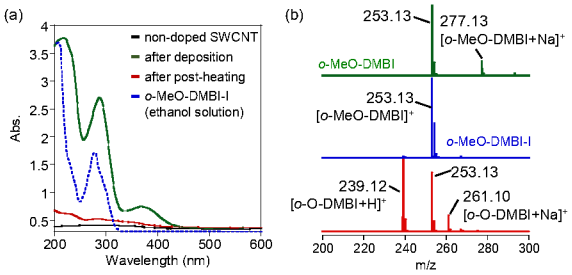

Fig. 4 (a) UV-vis-NIR spectra of non-doped SWCNT-coated quartz substrate (black), SWCNT-coated quartz substrate after *o*-MeO-DMBI-I deposition (green), and SWCNT-coated quartz substrate after deposition and post heating at 80 °C for 90 min (red). The spectra of *o*-MeO-DMBI-I in solution (ethanol) is also shown (blue). (b) Electrospray ionization (ESI) mass spectroscopy data of *o*-MeO-DMBI (green), *o*-MeO-DMBI-I (blue) and dissolved compounds from the deposited substrate (red).

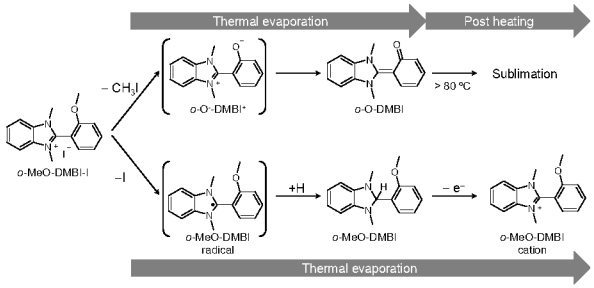

Scheme 1. Possible reactions routes of *o*-MeO-DMBI-I during thermal deposition under vacuum (10^{-3} Pa) at a heating temperature of 180 °C and post heating at 80 °C for 90 min. (upper route) Elimination of CH_3I followed by isomerization during thermal evaporation and sublimation during post heating. (lower route) Generation of radical induced by the removal of I followed by the formation of *o*-MeO-DMBI, which can dope SWCNTs to form *o*-MeO-DMBI cation during thermal evaporation.

To further study the doping reaction mechanism, the UV-vis-NIR absorption of the SWCNT sheets was characterized during the doping process. Fig. 4a displays the UV-vis-NIR absorption spectra of SWCNT-coated quartz substrates before and after *o*-MeO-DMBI-I deposition and post heating (80 °C for 90 min). A new peak appeared at approximately 370 nm after deposition (green line), which was also observed for *o*-MeO-DMBI-I deposited on quartz substrate without SWCNTs (Fig. S6†) but not observed for *o*-MeO-DMBI-I in solution (ethanol; blue dotted line). After post-heating, there was a large decrease in absorption (red line). Schwarze et al.[52] noted that the thermal deposition of *o*-MeO-DMBI-Cl yielded zwitterion compounds (*o*-O^--$DMBI^+$) via cleavage of the CH_3 group in $–OCH_3$ (Scheme S1†), and the sublimation of these doping-inactive compounds during post heating improved the doping efficiency. We considered that a similar reaction occurred for *o*-MeO-DMBI-I to generate *o*-O^--$DMBI^+$ zwitterions (Scheme 1).

To determine the molecular structure of the deposited compounds, the SWCNT sheets were dipped into ethanol after the thermal deposition process to dissolve the deposited compounds. The solution was then studied using electrospray ionization (ESI) mass spectroscopy. As shown in Fig. 4b (red spectrum), two main peaks were observed at m/z = 253.13 and 239.12. The peak at m/z = 239.12 was assigned to *o*-O^--$DMBI^+$ or its isomer (*o*-O-DMBI; see Scheme 1), which has a molecular weight of M_w = 238.11. Since zwitterions are generally thermally stable due to electrostatic interaction, we expect that nonionic *o*-O-DMBI was produced and evaporated during the post heating process, which might be the cause of the decrease in absorption at 370 nm (Fig. 4a). The second peak, at m/z = 253.13, was also observed for both *o*-MeO-DMBI-I and *o*-MeO-DMBI,[53] as shown in Fig. 4b (blue and green spectra, respectively). Therefore, it is likely to be generated from the *o*-MeO-DMBI radical (see Scheme 1). In addition, the *o*-MeO-DMBI cation may contribute to this peak. Because the XPS I 3d scans of the SWCNT sheets after thermal deposition (Fig. 2f,

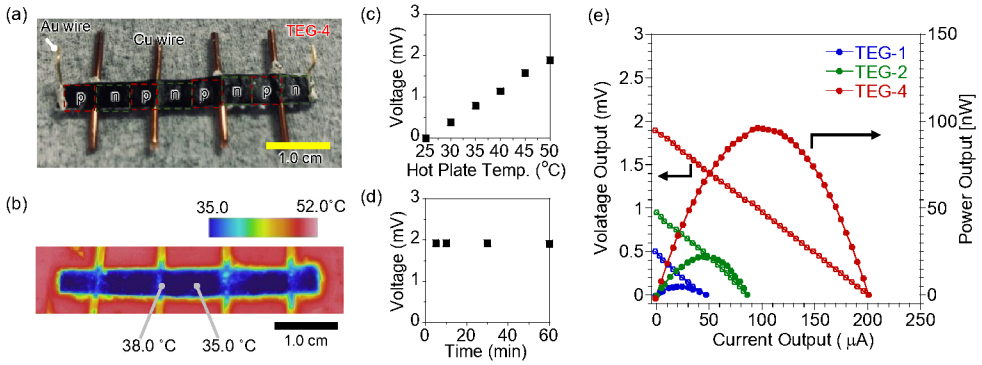

Fig. 5 (a) Top view photograph of TEG-4 (dimensions: 4.0 × 40 mm). (b) Temperature mapping of the TEG-4 on a hot plate at 50 °C. (c) Plot of OCV of TEG-4 as a function of hot plate temperature. (d) Time dependence of OCV for TEG-4 at a hot plate temperature of 50 °C. (e) Voltage output (open circles) and power output (filled circles) of TEG-1 (blue), TEG-2 (green), and TEG-4 (red) as a function of the current output.

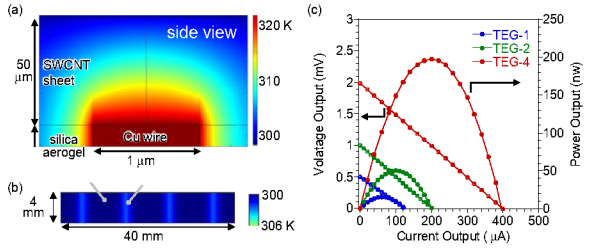

Fig. 6 (a) Side view of simulated temperature distribution at a p–n boundary. (b) Top view of simulated temperature distribution in TEG-4. (c) Simulated voltage output (open circles) and power output (filled circles) of TEG-1 (blue), TEG-2 (green), and TEG-4 (red).

green line) were lacking the I 3d peak, the presence of *o*-MeO-DMBI-I can be excluded. Bao et al.[47] conducted mass spectroscopy to identify the gaseous compounds that evaporated from *o*-MeO-DMBI-I and detected a compound with a molecular weight of M_w = 254.3, which they assigned as *o*-MeO-DMBI. Therefore, we consider that *o*-MeO-DMBI was formed from *o*-MeO-DMBI radicals during thermal evaporation, and the doping of the SWCNTs formed *o*-MeO-DMBI cations, which both produced an identical peak at m/z = 253.13. Further doping during post heating at 80 °C may proceed by the removal of *o*-O-DMBI, which would stabilize the *o*-MeO-DMBI cations on the negatively-charged SWCNTs. A similar increase in doping efficiency upon the removal of *o*-O-DMBI during post heating was also observed for thermally deposited *o*-MeO-DMBI-I on *N*, *N*-bis(fluoren-2-yl)-naphthalene tetracarboxylic diimide.[52]

For the n-doped SWCNT sheets, air stability has been the critical issue since the n-doped SWCNT sheets easily turned into p-type by air oxidation.[23] The air-stability of the doped SWCNT sheets was monitored by monitoring the Seebeck coefficient for 80 days and found the Seebeck coefficient was gradually changed from –55 to –40 μV K^{-1} after 80 days (Fig. S7†). We reported that the surface coverage of the SWCNTs by dopant cations was the key to achieve the air-stability.[35] In the deposition method, it is considered that the removal of *o*-O-DMBI formed defects of the dopant layer and allowed the slight oxidation.

Power output of planar TEGs

Planar SWCNT-based TEG devices with one, two, and four p–n sequences (denoted as TEG-1, TEG-2, and TEG-4, respectively) were fabricated by the patterning of SWCNT sheets via the thermal deposition and post heating method. Cu wires were attached at alternate p–n boundaries as a thermal conductor, while a thermal insulator (silica aerogel/poly(vinyl alcohol) composite[54]) was applied to the other areas of the surface (Fig. 5a, see also Fig. 1b). The devices were connected with Au wires to monitor the voltage and power output.

The TEG devices were placed on a hot plate set at 50 °C in the room controlled at 25 °C to generate a thermal gradient. Fig. 5b shows a thermogram of TEG-4. The temperature difference between the p–n boundaries with thermal conductors and thermal insulators was 3 °C. The open circuit voltage (OCV) linearly increased with the increase of the hot-plate temperature (Fig. 5c) and was stable for at least 1 h (Fig. 5d). In Fig. 5e, the voltage output (open circles) and power output (filled circles) are plotted for TEG-1 (red), TEG-2 (green), and TEG-4 (blue) as a function of the current output. The OCV and maximum power density increased linearly with the number of units (red plot in Fig. S8†), while the resistance of the device was constant (blue plot in Fig. S8†). The linear increase in power density without an increase in resistance is a key advantage of this structure. For TEG-4, the power output reached a maximum of 96.1 nW, corresponding to a power density of 60 nW cm^{-2}.

Table 1. Measured and simulated values of the open circuit voltage (OCV), power density, and circuit resistance of TEG-1, TEG-2, and TEG-4.

	OCV [mV]		Power density [nw]		Circuit resistance [Ω]	
	Measured	Simulated	Measured	Simulated	Measured	Simulated
TEG-1	0.468	0.497	4.852	15.40	10.50	5.000
TEG-2	0.954	1.000	22.01	50.30	10.71	5.000
TEG-4	1.983	1.990	96.09	198.0	9.336	5.000

To compare the efficiency of the devices with other SWCNT-based TEGs, the specific power generation capacity (ϕ) was calculated, determined as $\phi = p/(A\Delta T^2)$, where p, A, and ΔT are the maximum power [μW], area of heating [m^2 or cm^2], and applied temperature difference [K].[55] In the "energy harvesting mode" calculation, the temperature difference between the hot and cool sides (ΔT = 25 °C) was used, although the actual temperature difference at the boundary areas was 3 K, as shown in Fig. 5b. The obtained ϕ value for TEG-4 (0.96 μW m^{-2} K^{-2}) was relatively high compared to that of various SWCNT TEGs (Table S1†),[56-59] and higher than that of the recent silicon-based planar TEGs, which had a ϕ value of 0.062 μW m^{-2} K^{-2} in energy harvesting mode.[60] It should be noted that SWCNT-based TEGs with ϕ values higher than 10 μW m^{-2} K^{-2} (Table S1†)[39, 44] have been reported, and some silicon-based TEGs have exhibited ϕ values higher than 100 μW m^{-2} K^{-2}.[61] Therefore, further improvement is necessary to optimize SWCNT quality and/or TEG structure and to obtain TEGs that can compete with state-of-the-art devices.

To verify the power output of the planar SWCNT-based TEG devices, simulations were conducted based on the finite element method. The experimental data for electrical conductivity, Seebeck coefficient, and thermal conductivity at temperatures of 50 and 25 °C were used for the hot and cool sides, respectively. Fig. 6a shows a side view of the simulated sheet at the boundary of the p- and n-type regions. The temperature gradient was generated in both the in-plane and through-plane directions. In the top view image of the simulated TEG-4 (Fig. 6b), the temperature distribution was in good agreement with the thermogram shown in Fig. 5b. The simulated OCV values of the TEGs were also well reproduced (Fig. 6c and Table 1). However, there was an approximately 5 Ω difference between the simulated and measured resistance

values, which may be due to the contact resistance at the Au electrode.

It should be emphasized that our device structure can be easily scaled without increasing the size of the TEG module by decreasing the pattern size. The good agreement between the simulated and experimental results demonstrates that the TEG design can be optimized through simulation, reducing the need for timely and costly experimentation. Such optimization is currently ongoing in our group. Ferguson et al.[23] pointed out that the power factor over 1000 $\mu W\ m^{-1}\ K^{-2}$ was obtained from the SWCNT sheets prepared without sonication mainly due to the remarkable electrical conductivity over 1000 $S\ cm^{-1}$. Therefore, large improvement of the performance is expected when our method is applied for these sheets.

Conclusions

In summary, the thermal deposition of *o*-MeO-DMBI-I with post heating resulted in the successful n-doping of a 50-μm-thick p-type SWCNT sheet. Precise p–n patterning was achieved by using a slit mask. The lateral diffusion of dopant molecules was limited to ca. 100 μm, which is considerably smaller than that with solution-based doping processes (diffusion length of a few centimeters). Planar SWCNT-based TEG devices were fabricated via p–n patterning based on the thermal deposition method, with thermal conductors attached at alternate p–n junctions. A power density of 60 $nW\ cm^{-2}$ was achieved at a temperature difference of 25 °C was applied for the device with four integrated p–n units. The power density of devices with this planar structure can be increased further through simulation-based design to optimize the pattern width, SWCNT sheet thickness, and so on. This optimization work is currently ongoing.

Experimental

Materials. SWCNTs (Meijo-eDIPS) with a diameter of 1.5 ± 0.5 nm were purchased from Meijo Nano Carbon. Ethanol and *N*-methylpyrrolidone (NMP) were purchased from FUJIFILM Wako Pure Chemicals Corp (Tokyo, Japan). Methanol was purchased from Kanto Chemical (Tokyo, Japan). Silica aerogel (ENOVA, IC3110) and poly(vinyl alcohol) were purchased from Cabot Corp (Boston, USA) and MilliporeSigma (St. Louis, USA), respectively. 2-(2-Methoxyphenyl)-1,3-dimethyl-1*H*-benzoimidazol-3-ium iodide (*o*-MeO-DMBI-I) was synthesized according to a modified method based on previous reports (Scheme S2).[35]

Characterization. X-ray photoelectron spectroscopy was conducted at room temperature using an AXIS-ULTRA spectrometer (Shimadzu, Kyoto Japan), in which indium was used as the substrate. Scanning electron microscopy (SEM) was carried out using an SU-9000 microscope (Hitachi High Technologies, Tokyo Japan) with an accelerating voltage of 5.0 kV. Optical absorption measurements were performed using a V-670 spectrophotometer (JASCO, Tokyo Japan). The in-plane electrical conductivity and in-plane Seebeck coefficient were measured using a ZEM-3 measurement system (ADVANCE RIKO, Yokohama Japan) under a helium atmosphere at ~0.01 MPa from 30 to 100 °C. Through-plane mapping of the Seebeck coefficient and thermal conductivity were conducted via scanning thermal probe microimaging (STPM-1000, ADVANCE RIKO, Yokohama Japan), where the 10 × 10 mm area was scanned in 0.2 × 0.2 mm pitch (50 × 50 spots; 2500 measurement spots in total). The temperature of the SWCNT sheet was monitored using an InfReC R450 thermal imaging camera (NIPPPON AVIONICS CO., LTD. Yokohama Japan). Electrospray ionization mass spectroscopy was conducted using an AccuTOF LC-plus 4G system (JEOL, Tokyo Japan).

Fabrication of SWCNT sheets. SWCNTs (65.0 mg) were dispersed in NMP (650 mL) using a bath-type sonicator (Branson 5010) for 2 h. Further NMP (325 mL) was then added, followed by sonication for 1 h. The dispersion was filtered through a polytetrafluoroethylene membrane (pore diameter: 1.0 μm). The obtained sheet was removed from the membrane and washed by dipping it in methanol to remove residual NMP, followed by vacuum-drying at 80 °C for 8 h. The thickness of the sheets was 50 μm. The free-standing SWCNT sheets were cut by scissors to the specified size.

Fabrication of SWCNT-coated quartz substrate. SWCNTs (1.0 mg) were suspended in ethanol (20 mL) by sonication in a bath-type sonicator for 1 h. The SWCNT suspension was dropped on a quartz substrate (70 × 8.0 mm).

Doping of SWCNTs by o-MeO-DMBI-I based on thermal deposition method. The non-doped SWCNT sheet attached on the sample holder was covered by a patterned slit mask (stainless sheet: 1 mm thick) and placed in a vacuum chamber (VPC-260, ULVAC, Tokyo Japan). *o*-MeO-DMBI-I was placed in a tungsten boat and heated at 180 °C under vacuum (10^{-3} Pa). The temperature of the boat was measured using a K-type thermocouple. After the thermal vapor deposition of *o*-MeO-DMBI-I, the SWCNT sheet was post heated at 80 °C under vacuum for 90 min. After the post-heating, the doped sheet was taken from the chamber and used for the measurements.

Fabrication of planar SWCNT-based TEGs. Cu wire (diameter: 1.0 mm) was attached at the boundary between the p- and n-doped regions on one side of the SWCNT sheet. The other areas of the sheet surface were passivated using a silica aerogel/poly(vinyl alcohol) composite insulator.[54] Au wire was connected to both ends of the SWCNT sheet using Ag paste. The *I*–*V* performance was measured using a Keithley 2401 source meter (Tektronix, Tokyo Japan).

Author Contributions

The manuscript was written through contributions of all authors. All authors have given approval to the final version of the manuscript.

Conflicts of interest

There are no conflicts to declare.

Acknowledgements

We thank to Dr. Daichi Suzuki for useful discussion of the measurements. This study was supported in part by the Nanotechnology Platform Project of the Ministry of Education, Culture, Sports, Science and Technology (MEXT), Japan, KAKENHI (No. JP18H01816), the bilateral program (JPJSBP120208814) of the Japan Society for the Promotion of Science (JSPS), PRESTO (No. JPMJPR15R6), and CREST (No. JPMJCR19Q5) of the Japan Science and Technology Agency (JST), Japan. We also thank Dr. Maho Yoshiizumi (ADVANCE RIKO, Yokohama Japan) for the Seebeck coefficient mapping measurements.

Notes and references

1. L. Gao, Y. Zhang, V. Malyarchuk, L. Jia, K. I. Jang, R. C. Webb, H. Fu, Y. Shi, G. Zhou, L. Shi, D. Shah, X. Huang, B. Xu, C. Yu, Y. Huang and J. A. Rogers, *Nat Commun*, 2014, **5**, 4938.
2. R. C. Webb, Y. Ma, S. Krishnan, Y. Li, S. Yoon, X. Guo, X. Feng, Y. Shi, M. Seidel and N. H. Cho, *Sci. Adv.*, 2015, **1**, e1500701.
3. A. Tricoli, N. Nasiri and S. De, *Adv. Funct. Mater.*, 2017, **27**, 1605271.
4. P. J. Taroni, G. Santagiuliana, K. Wan, P. Calado, M. Qiu, H. Zhang, N. M. Pugno, M. Palma, N. Stingelin‐Stutzman and M. Heeney, *Adv. Funct. Mater.*, 2018, **28**, 1704285.
5. R. C. Webb, A. P. Bonifas, A. Behnaz, Y. Zhang, K. J. Yu, H. Cheng, M. Shi, Z. Bian, Z. Liu and Y.-S. Kim, *Nat. Mater.*, 2013, **12**, 938-944.
6. J. P. Giraldo, H. Wu, G. M. Newkirk and S. Kruss, *Nat. Nanotech.*, 2019, **14**, 541-553.
7. W. Zeng, L. Shu, Q. Li, S. Chen, F. Wang and X. M. Tao, *Adv. Mater.*, 2014, **26**, 5310-5336.
8. L. Yang, Z. G. Chen, M. S. Dargusch and J. Zou, *Adv. Energy Mater.*, 2018, **8**, 1701797.
9. B. Dörling, J. D. Ryan, J. D. Craddock, A. Sorrentino, A. E. Basaty, A. Gomez, M. Garriga, E. Pereiro, J. E. Anthony and M. C. Weisenberger, *Adv. Mater.*, 2016, **28**, 2782-2789.
10. S. J. Kim, J. H. We and B. J. Cho, *Energy Environ. Sci*, 2014, **7**, 1959-1965.
11. S. Perumal, S. Roychowdhury, D. S. Negi, R. Datta and K. Biswas, *Chem. Mater.*, 2015, **27**, 7171-7178.
12. C. J. Vineis, A. Shakouri, A. Majumdar and M. G. Kanatzidis, *Adv. Mater.*, 2010, **22**, 3970-3980.
13. Y.-L. Pei, H. Wu, D. Wu, F. Zheng and J. He, *J. Am. Chem. Soc.*, 2014, **136**, 13902-13908.
14. L.-D. Zhao, J. He, S. Hao, C.-I. Wu, T. P. Hogan, C. Wolverton, V. P. Dravid and M. G. Kanatzidis, *J. Am. Chem. Soc.*, 2012, **134**, 16327-16336.
15. Z. Chen, Z. Jian, W. Li, Y. Chang, B. Ge, R. Hanus, J. Yang, Y. Chen, M. Huang and G. J. Snyder, *Adv. Mater.*, 2017, **29**, 1606768.
16. K. Peng, X. Lu, H. Zhan, S. Hui, X. Tang, G. Wang, J. Dai, C. Uher, G. Wang and X. Zhou, *Energy Environ. Sci*, 2016, **9**, 454-460.
17. D. Bao, J. Chen, Y. Yu, W. Liu, L. Huang, G. Han, J. Tang, D. Zhou, L. Yang and Z.-G. Chen, *Chem. Eng. J.*, 2020, **388**, 124295.
18. L. Wang, J. Li, C. Zhang, T. Ding, Y. Xie, Y. Li, F. Liu, W. Ao and C. Zhang, *J. Mater. Chem. A*, 2020, **8**, 1660-1667.
19. L. Hu, F. Meng, Y. Zhou, J. Li, A. Benton, J. Li, F. Liu, C. Zhang, H. Xie and J. He, *Adv. Funct. Mater.*, 2020, 2005202.
20. I. T. Witting, T. C. Chasapis, F. Ricci, M. Peters, N. A. Heinz, G. Hautier and G. J. Snyder, *Adv. Electron. Mater.*, 2019, **5**, 1800904.
21. K. Fukuie, Y. Iwata and E. Iwase, *Micromachines*, 2018, **9**, 315.
22. N. Nandihalli, C.-J. Liu and T. Mori, *Nano Energy*, 2020, **78**, 105186.
23. J. L. Blackburn, A. J. Ferguson, C. Cho and J. C. Grunlan, *Adv. Mater.*, 2018, **30**, 1704386.
24. T. Fujigaya, *Bull. Chem. Soc. Jpn.*, 2019, **92**, 400-408.
25. Y. Nonoguchi, K. Ohashi, R. Kanazawa, K. Ashiba, K. Hata, T. Nakagawa, C. Adachi, T. Tanase and T. Kawai, *Sci. Rep.*, 2013, **3**.
26. R. Chen, J. Tang, Y. Yan and Z. Liang, *Adv. Mater. Technol.*, 2020, 2000288.
27. S. L. Kim, K. Choi, A. Tazebay and C. Yu, *ACS nano*, 2014, **8**, 2377-2386.
28. C. A. Hewitt, A. B. Kaiser, S. Roth, M. Craps, R. Czerw and D. L. Carroll, *Nano Lett.*, 2012, **12**, 1307-1310.
29. S. Kim, J.-H. Mo and K.-S. Jang, *ACS Appl. Mater. Interfaces*, 2019, **11**, 35675-35682.
30. T. Watanabe, S. Asada, T. Xu, S. Hashimoto, S. Ohba, Y. Himeda, R. Yamato, H. Zhang, M. Tomita and T. Matsukawa, 2017 IEEE Electron Devices Technology and Manufacturing Conference (EDTM), Toyama, Japan, 2017.
31. J. Tang, Y. Chen, S. R. McCuskey, L. Chen, G. C. Bazan and Z. Liang, *Adv. Electron. Mater.*, 2019, **5**, 1800943.
32. Y. Nonoguchi, M. Nakano, T. Murayama, H. Hagino, S. Hama, K. Miyazaki, R. Matsubara, M. Nakamura and T. Kawai, *Adv. Funct. Mater.*, 2016, **26**, 3021-3028.
33. D. Suzuki, Y. Ochiai, Y. Nakagawa, Y. Kuwahara, T. Saito and Y. Kawano, *ACS Appl. Nano Mater.*, 2018, **1**, 2469-2475.
34. B. D. Naab, S. Zhang, K. Vandewal, A. Salleo, S. Barlow, S. R. Marder and Z. Bao, *Adv. Mater.*, 2014, **26**, 4268-4272.
35. Y. Nakashima, R. Yamaguchi, F. Toshimitsu, M. Matsumoto, A. Borah, A. Staykov, M. S. Islam, S. Hayami and T. Fujigaya, *ACS Appl. Nano Mater.*, 2019, **2**, 4703-4710.
36. Q. Hu, Z. Lu, Y. Wang, J. Wang, H. Wang, Z. Wu, G. Lu, H.-L. Zhang and C. Yu, *J. Mater. Chem. A*, 2020, **8**, 13095-13105.
37. X. Yin, F. Zhong, Z. Chen, C. Gao, G. Xie, L. Wang and C. Yang, *Chem. Eng. J.*, 2020, **382**, 122817.
38. Q. Hu, Z. Lu, Y. Wang, J. Wang, H. Wang, Z. P. Wu, G. Lu, H.-L. Zhang and C. Yu, *J. Mater. Chem. A*, 2020.
39. W. Zhou, Q. Fan, Q. Zhang, L. Cai, K. Li, X. Gu, F. Yang, N. Zhang, Y. Wang, H. Liu, W. Zhou and S. Xie, *Nat. Commun.*, 2017, **8**, 14886.
40. K. Chatterjee, A. Negi, K. Kim, J. Liu and T. K. Ghosh, *ACS Applied Energy Materials*, 2020, **3**, 6929-6936.
41. T. Fukumaru, T. Fujigaya and N. Nakashima, *Sci. Rep.*, 2015, **5**.
42. C. J. An, Y. H. Kang, H. Song, Y. Jeong and S. Y. Cho, *J. Mater. Chem. A*, 2017, **5**, 15631-15639.

43. M. H. Lee, Y. H. Kang, J. Kim, Y. K. Lee and S. Y. Cho, *Adv. Energy Mater.*, 2019, **9**, 1900914.
44. T. Sun, B. Zhou, Q. Zheng, L. Wang, W. Jiang and G. J. Snyder, *Nat. Commun.*, 2020, **11**, 1-10.
45. H. Wang, P. Wei, Y. Li, J. Han, H. R. Lee, B. D. Naab, N. Liu, C. Wang, E. Adijanto and B. C.-K. Tee, *Proc. Natl. Acad. Sci. U. S. A.*, 2014, **111**, 4776-4781.
46. Z. Bin, L. Duan and Y. Qiu, *ACS Appl. Mater. Interfaces*, 2015, **7**, 6444-6450.
47. P. Wei, T. Menke, B. D. Naab, K. Leo, M. Riede and Z. Bao, *J. Am. Chem. Soc.*, 2012, **134**, 3999-4002.
48. R. Graupner, J. Abraham, A. Vencelova, T. Seyller, F. Hennrich, M. M. Kappes, A. Hirsch and L. Ley, *Phys. Chem. Chem. Phys.*, 2003, **5**, 5472-5476.
49. P. Wei, N. Liu, H. R. Lee, E. Adijanto, L. Ci, B. D. Naab, J. Q. Zhong, J. Park, W. Chen, Y. Cui and Z. Bao, *Nano Lett.*, 2013, **13**, 1890-1897.
50. T. M. L., R. B. D., S. Martin, F. Axel, R. Steffen, B. N. Jan, L. Björn, L. Karl and B. Jean‐Luc, *Adv. Funct. Mater.*, 2016, **26**, 3730-3737.
51. Y. Hirana, G. Juhasz, Y. Miyauchi, S. Mouri, K. Matsuda and N. Nakashima, *Sci. Rep.*, 2013, **3**.
52. M. Schwarze, B. D. Naab, M. L. Tietze, R. Scholz, P. Pahner, F. Bussolotti, S. Kera, D. Kasemann, Z. Bao and K. Leo, *ACS Appl. Mater. Interfaces*, 2018, **10**, 1340-1346.
53. Y. Nakashima, N. Nakashima and T. Fujigaya, *Synth. Met.*, 2017, **225**, 76-80.
54. H. M. Kim, Y. J. Noh, J. Yu, S. Y. Kim and J. R. Youn, *Composites Part A*, 2015, **75**, 39-45.
55. G. Hu, H. Edwards and M. Lee, *Nature Electronics*, 2019, **2**, 300-306.
56. K. Suemori, S. Hoshino and T. Kamata, *Appl. Phys. Lett.*, 2013, **103**, 153902.
57. C.-K. Mai, B. Russ, S. L. Fronk, N. Hu, M. B. Chan-Park, J. J. Urban, R. A. Segalman, M. L. Chabinyc and G. C. Bazan, *Energy Environ. Sci*, 2015, **8**, 2341-2346.
58. M. Ito, T. Koizumi, H. Kojima, T. Saito and M. Nakamura, *J. Mater. Chem. A*, 2017, **5**, 12068-12072.
59. G. Wu, Z.-G. Zhang, Y. Li, C. Gao, X. Wang and G. Chen, *ACS Nano*, 2017, **11**, 5746-5752.
60. A. George, R. Yanagisawa, R. Anufriev, J. He, N. Yoshie, N. Tsujii, Q. Guo, T. Mori, S. Volz and M. Nomura, *ACS Appl. Mater. Interfaces*, 2019, **11**, 12027-12031.
61. B. M. Curtin, E. W. Fang and J. E. Bowers, *J. Electron. Mater.*, 2012, **41**, 887-894.